three dimensional Direct Numerical Simulation of Soot Formation and Transport in a Temporally-Evolving Nonpremixed Ethylene Jet Flame

David O. Lignell[a,*], Jacqueline H. Chen[a], Philip J. Smith[b]

[a] *Reacting Flow Research Department, Combustion Research Facility, Sandia National Laboratories, Livermore, CA 94551*
[b] *Department of Chemical Engineering, The University of Utah, Salt Lake City, UT 84098*

Abstract

three dimensional direct numerical simulation of soot formation with complex chemistry is presented. The simulation consists of a temporally-evolving, planar, nonpremixed ethylene jet flame with a validated, 19-species reduced mechanism. A four-step, three-moment, semi-empirical soot model is employed. Previous two dimensional decaying turbulence simulations have shown the importance of multidimensional flame dynamical effects on soot concentration [Lignell et al. *Combust. Flame* 151 (2007) 2-28]. It was shown that flame curvature strongly impacts the diffusive motion of the flame relative to soot (which is essentially convected with the flow), resulting in soot being differentially transported toward or away from the flame zone. The proximity of the soot to the flame directly influences soot reactivity and radiative properties. Here, the analysis is extended to three dimensions in a temporal jet configuration with mean shear. Results show that similar local flame dynamic effects of strain and curvature are important, but that enhanced turbulent mixing of fuel and oxidizer streams has a first-order effect on transport of soot towards flame zones. Soot modeling in turbulent flames is a challenge due to the complexity of soot formation and transport processes, and the lack of detailed experimental soot-flame-flow structural data. The present DNS provides the first step towards providing such data.

Keywords: soot, DNS, nonpremixed, turbulent combustion, ethylene, jet flame

1. Introduction

Soot formation in turbulent hydrocarbon combustion is of great practical importance. Soot emission is a known health hazard, and its presence indicates reduced combustion efficiency. Soot formation is responsible for the bulk of flame luminosity and radiative heat transfer. For these reasons, and others, soot formation in laminar and turbulent flames is a subject of ongoing research. Soot formation in flames, particularly turbulent flames, is a complex process involving a rich set of physical phenomena that make experimental and computational investigation challenging. Some of the difficulties are

- Soot formation chemistry involves a large number of increasingly high molecular weight species: notably formation and growth involving PAH [1].
- Soot exists as a particle phase with a continuous size distribution, which must be accounted for in conjunction with the gas-phase chemistry [2, 3].
- Flames with substantial soot concentrations can be optically thick with respect to radiative heat transfer [4, 5].
- Transport of soot occurs primarily via thermophoresis, and, as a particle phase, soot is transported differentially to gaseous species [6, 7].
- The time scales of soot formation are longer than typical combustion time scales, resulting in overlap of soot chemistry and large-scale flow features [8, 9].

Many detailed analyses of soot-flame interactions have been performed that characterize soot concentration, temperature, particle size distribution, and relevant chemical flow fields [3, 4, 10, 11, 12, 13]. However, these detailed experimental and computational studies have been limited mainly to well-characterized, canonical configurations in laminar, steady (and some unsteady) flows. Experimental studies of turbulent sooting flames are limited to providing statistical quantities (e.g., means of soot volume fraction and number density), and cannot resolve detailed flame-soot-flow structural interactions due to the optical thickness of the flames and the thin structures of the soot layers. Large-scale turbulent simulations using RANS or LES approaches use subgrid models adapted to soot formation [7, 14], but detailed soot-flame structure data in turbulent environments is not available for model development and validation.

Direct numerical simulation (DNS) resolves all relevant flow and chemical species time scales and length scales, and is currently the only feasible method that can provide details of the full spatial and temporal reacting flow

*Corresponding author
Email address: david@crsim.utah.edu (David O. Lignell)

field. DNS of turbulent flames with soot formation has recently been performed in two dimensions [15, 16]. Here, we extend reacting DNS with realistic gas-phase chemistry and soot formation to three dimensional turbulent flames. The goal of the DNS simulations is twofold: (1) to provide detailed data that can be used to develop and validate subgrid chemistry models for large-scale practical applications, and (2), to gain fundamental physical insight into soot-flame-flow interactions. As discussed in more detail below, the DNS configuration consists of a temporally-evolving, non-premixed ethylene jet flame with a validated 19-species reduced ethylene mechanism, and a 4-step, 3-moment, semi-empirical soot model.

We recently performed two dimensional simulations of soot formation in decaying turbulence to study the effects of unsteady, multidimensional flame dynamics on soot formation and transport processes [16]. There, it is shown that differential diffusion between the soot and the flame determines the proximity of the soot to the flame, and hence the temperature and composition environment of the soot. These, in turn, directly influence rates of soot reaction (hence concentration) and radiative emission.

Soot transport occurs primarily via convection and thermophoresis, while flame surface motion (e.g., the motion of the stoichiometric mixture fraction surface) occurs via diffusion and convection. The relative motion between soot and the flame zone was previously quantified by examining the flame motion relative to convection, termed the *flame displacement velocity*, v_ξ [16]. Since soot is mainly convected with the flow, the sign of v_ξ determines whether soot is convected into, or away from the high temperature flame. This velocity derives from two terms: a *flame curvature term*, and diffusion resolved in the direction normal to the flame surface, referred to as the *normal diffusion term*. It was found in the two dimensional study that both terms are important [16]. The curvature term is inherently multidimensional, while the normal diffusion term is one dimensional. It was further found that up to 15% of the flow experiences regions of both signs of v_ξ. In regions where the center of flame curvature is in the fuel stream, the flame motion is shifted in the direction of the fuel stream (so that soot is convected towards the flame, resulting in higher soot concentrations), and vice-versa. These flame dynamic effects are not directly included in RANS and LES simulations involving soot formation, so quantification of these effects is important.

In this paper, we extend the previous analysis to a three dimensional jet configuration. Unlike the two dimensional decaying turbulence simulation [16], significantly higher mixing rates occur in the present shear driven turbulent jet. The enhanced bulk mixing of fuel and oxidizer impacts the mixture fraction PDF and the soot transport in the mixture fraction coordinate through the governing transport terms. We present results of the three dimensional simulation, statistics of the flame displacement velocity and its contributing terms, and quantify the role of the thermophoretic diffusion velocity.

2. Numerical Implementation

The ethylene jet simulation was performed using S3D, a massively parallel DNS code developed at Sandia National Laboratories. S3D solves the reacting, compressible Navier-Stokes equations using an explicit fourth-order, low-storage Runge-Kutta algorithm [18]. Spatial derivatives are approximated with eighth-order central differences on a uniform Cartesian grid. A tenth-order spatial filter is applied at each timestep to remove high wavenumber content and reduce aliasing errors [19]. Composition- and temperature-dependent thermodynamic and transport properties are evaluated using the Chemkin [20] and Transport programs [21]. Thermal conductivity, viscosity, and gaseous species diffusion fluxes are computed with a mixture averaged formulation, with effective diffusivities used for species diffusion coefficients.

2.1. Ethylene Combustion Mechanism

A reduced ethylene combustion mechanism was developed from a detailed mechanism consisting of 70 species and 463 reactions [22]. The detailed mechanism was reduced using the directed relation graph method, sensitivity analysis and computational singular perturbation [16]. The following 19 transported species are included in the mechanism (along with ten other quasi-steady-state species): H_2, H, O, O_2, OH, H_2O, HO_2, H_2O_2, CH_3, CH_4, CO, CO_2, CH_2O, C_2H_2, C_2H_4, C_2H_6, CH_2CO, C_3H_6, N_2. The mechanism was extensively validated for all combustion conditions experienced in the present DNS. These validations consisted of ignition delay, extinction residence time in a perfectly stirred reactor, laminar flame speed, and species concentration profiles in one dimensional non-premixed counterflow diffusion flames [16]. The reduced chemical mechanism is tailored to multidimensional flow simulation in that it minimizes the number of chemical species that must be transported. In addition, the chemical stiffness is reduced through the use of quasi-steady-state species assumptions, allowing time-step sizes that are limited by acoustics and not by fast chemical time scales. The quasi-steady-state species concentrations are computed without the need for nonlinear iteration, which improves computational stability and efficiency. The reduction strategy employed enables DNS with complex chemistry representing increasingly complex hydrocarbon fuels, e.g., in this case ethylene. The reduced mechanism provides a speedup factor of approximately two orders of magnitude compared to the detailed mechanism it is derived from.

2.2. Soot Model

The soot model is based on Leung and Lindstedt [10], which has been used extensively in simulations of turbulent sooting flames. This model is a semi-empirical, four-step model consisting of nucleation, growth, oxidation, and coagulation. Acetylene is the gaseous species through which soot nucleation and surface growth occurs. Soot oxidation

occurs in a global reaction in terms of O_2 concentration, with effects of oxidation via species such as OH and O partially built-in to the rate. While more complex soot chemistry models are available, such as the HACA mechanism [23], the present mechanism has been widely and successfully used in nonpremixed combustion and is considered adequate for the present purposes in which soot is introduced to three dimensional DNS.

The soot particle size distribution (PSD) is modeled using the method of moments, in which the first three mass-moments of the PSD are transported. The derivation of the moment transport equations results in fractional moments in the chemical source terms that are closed using an assumed-shape lognormal distribution [24]. This assumption was compared with quadrature closures [25] using four and six moments with good agreement between the models for the first two moments. The soot model is fully integrated into the gas-phase mechanism by accounting for mass and energy transfer between the gas and soot phases. Soot particles are small enough that they do not impact the fluid momentum (the Stokes number is much less than unity), and are convected with the flow. Soot diffusion occurs primarily via thermophoresis as given by

$$j_{Mr} = -0.554 M_r \frac{\nu}{T} \nabla T, \tag{1}$$

where M_r is the r^{th} soot moment, T is temperature, ν is kinematic viscosity, and j is the diffusion flux. Soot particles have a high molecular weight, and Brownian diffusion, while implemented [16], is insignificant [6, 7].

Soot and gaseous radiation is accounted for using an optically thin model, although radiative effects are negligible for the domain size, run time, and soot concentrations of the simulation. This was shown in two dimensions where longer time scales, length scales, and soot concentrations were present [16].

2.3. Initial Conditions and Configuration

The DNS consists of a temporally-evolving, nonpremixed, planar ethylene jet flame. A layer of fuel in the domain center is surrounded by counter-flowing oxidizer. The fuel slab extends to the full range of the stream-wise and span-wise directions, which are periodic. The cross-stream boundary conditions are open, with non-reflecting outflow boundary conditions [26]. The mean flow is one dimensional in the cross-stream direction and pressure, which is initialized to 1 atm, is approximately constant throughout the simulation. This configuration is optimal for model development because it is representative of shear-driven turbulent flows, maximizes the residence time of the fluid in the domain (for soot growth), and provides two homogeneous flow directions for turbulence statistics.

Physical parameters characterizing the simulation are presented in Table 1. The configuration was designed to balance competing computational costs associated with grid resolution (number of grid cells), total computational run time (which dictates the number of time steps and the soot reaction time), domain size (maximize Reynolds number and turbulence-flame interactions), and flame extinction (to be minimized). The fuel core width, H, is 1.8 mm, and the difference in velocity streams, ΔU is 82 m/s, giving a jet Reynolds number of 3700, based on the kinematic viscosity of the fuel stream. While the Reynolds number of the present flow is moderate, it is in the range of values studied in nonreacting, turbulent slot-jet experiments [27]. The simulation was run for 50 jet times, τ_j, defined by H and ΔU. The size of the domain is $16H \times 11H \times 6H$ in the stream-wise, cross-stream, and span-wise directions, respectively. A grid size of 30 μm was used in each direction, giving a total of 228 million computational grid cells.

The simulation is well-resolved for the mass, momentum, energy, and chemical species fields, with a minimum of 10 grid points across the thinnest radical species structures (i.e., a peak in the profile of a cross-stream cut). Experience and analytic tests have shown that good spatial resolution is achieved with 8-10 points across fine structures of transported scalars. The soot moment fields are less well-resolved with most of the thin structures containing at least five points. The choice of grid resolution was made on the basis of accuracy versus computational cost. The cost of the simulation scales as roughly the fourth power of the grid cell size precluding extensive resolution studies in three dimensions. A two dimensional resolution test was performed on 16 and 32 μm grids in a temporal jet configuration with similar parameters to those in Table 1: the jet height, stoichiometric mixture fraction and velocity difference were 1.5 mm, 0.2, and 75 m/s, respectively. Instantaneous velocity, temperature, and all gaseous species were nearly identical on the two grids whereas soot showed some variation. The mean relative error in the conditional (on mixture fraction) mean and standard deviation of soot mass fraction was 6% and 2%, respectively, between the two grids.

The fuel core velocity is perturbed with three dimensional isotropic, homogeneous turbulence intended to trip instabilities in the shear layers between the fuel and the oxidizer streams. The turbulence was initialized with $u'/\Delta U = 4\%$, and $H/L_{11} = 3$, where $u'/\Delta U$ is the turbulence intensity and L_{11} is the integral length scale. These parameters were used to define the velocity field satisfying the Passot-Pouquet turbulence kinetic energy spectrum [16, 28].

The chemical composition of the flow field is initialized by specifying a mixture fraction profile and mapping to this profile the composition and temperature fields of a one dimensional, steady laminar flamelet (SLF) solution. The mixture fraction ξ varies between zero in the oxidizer stream and unity in the fuel stream, with hyperbolic tangent transitions between the streams. The SLF solution was computed with a composition- and temperature-dependent scalar dissipation rate profile matching the mixture fraction profile in the DNS domain [16]. The transition width corresponds to 50% of the value at extinction.

Table 1: Temporal ethylene jet simulation parameters.

H (mm)	1.8	L_x/H	16	τ_{jet}	0.022
ΔU (m/s)	82	L_y/H	11	τ_{run}/τ_{jet}	50
Re_{jet}	3700	L_z/H	6	# Cells (millions)	228
$u'/\Delta U$ (init)	4%	Δx (μm)	30	Sim. Cost (million cpuh)	1.5
H/L_{11} (init)	3	δ_ξ (mm)	0.8		

Table 2: Stream compositions and temperatures.

Fuel, $\xi = 1$	X_{C2H4}	0.2546
	X_{N2}	0.7454
	T (K)	550
Oxidizer, $\xi = 0$	X_{O2}	0.2641
	X_{N2}	0.7359
	T (K)	550

Table 2 gives the compositions of the pure streams. The stoichiometric mixture fraction is 0.25. The compositions of initially pure ethylene and air streams are varied by moving nitrogen from the air stream to the fuel stream, hence maintaining a constant adiabatic flame temperature [29]. The increased stoichiometric mixture fraction ξ_{st} of 0.25, compared to 0.064 for pure fuel and air streams, increases the steady, stoichiometric, extinction scalar dissipation rate from 311 to 2554 s^{-1}, and moves the flame location closer to the turbulent shear layer. The stream temperatures were both preheated to 550 K. Preheating serves to make the flame more robust towards extinction, and reduces the density ratio between the burned and unburnt mixtures from 8.0 (with streams at 300 K) to 4.6. The lower density ratio and more robust flame provides a greater degree of flame-turbulence interaction than would otherwise be possible under the time and spatial resolution constraints of the DNS.

The simulation was performed on the Redstorm supercomputer at Sandia National Laboratories. A total of 7,920 processors were used, at a cost of 1.5 million cpuhours.

3. Results

The DNS results are presented in terms of (1) conditional statistics of gaseous combustion and soot scalars; (2) transport of soot relative to the flame in terms of the flame displacement velocity relative to convection, where the component terms of this velocity are quantified; (3) the relative importance of the thermophoretic diffusion velocity.

3.1. Overview

Figure 1 presents isocontour plots of temperature and soot mass fraction at $t = 50\tau_j$ for which significant development and mixing of the jet has occurred. At this time, the soot concentration is at its maximum level during the simulation and has undergone substantial flame and turbulence interactions. On the right are spanwise cuts corresponding to a plane in the streamwise and cross-stream directions with the initial fuel velocity moving towards the right, and the surrounding counter-flowing oxidizer streams moving towards the left. On the left are axial cuts showing the cross-stream and spanwise directions. As the simulation progresses in time, the turbulent shear layers develop and the jet spreads outwards in the cross-stream direction. The flame location also spreads outwards as expansion associated with combustion pushes fluid out of the domain. This figure illustrates the flow configuration and global flame characteristics. There is very little flame extinction occurring, although the flame is highly strained in the so-called "braid" regions between large-scale vortex structures. A key observation is the difference in the small-scale structure of the temperature field and the soot field. The temperature field is much more diffuse than the soot mass fraction field. All of the soot moments are qualitatively similar in appearance to the soot mass fraction ($M_1 = \rho Y_{soot}$). The soot diffusivity occurs primarily via thermophoresis and results in very thin structures. Soot is formed and grows on the fuel-rich side of the flame surface. Turbulent eddies strain the soot and convect it into the jet core where it mixes with combustion products and fuel. As discussed below, in the jet core region, the local mixture fraction surrounding the soot increases, while soot temperature and reaction rates are reduced.

3.2. Conditional Means and Scatter

The combustion and flow characteristics of the ethylene jet are quantified in Figure 2. This figure presents scatter data from the DNS at $t = 50\tau_j$, as well as the conditional (on mixture fraction) mean and conditional standard deviation as a function of mixture fraction. The mixture fraction computed and used throughout corresponds to the definition of Bilger [30]. The soot mass is not included in the calculation of the mixture fraction as the soot concentration is small compared to local elemental carbon concentrations. The figure presents temperature, scalar dissipation rate, OH mass fraction (indicative of the flame zone and reactivity) and acetylene (the soot precursor) mass fraction.

At earlier times, the results are qualitatively similar to

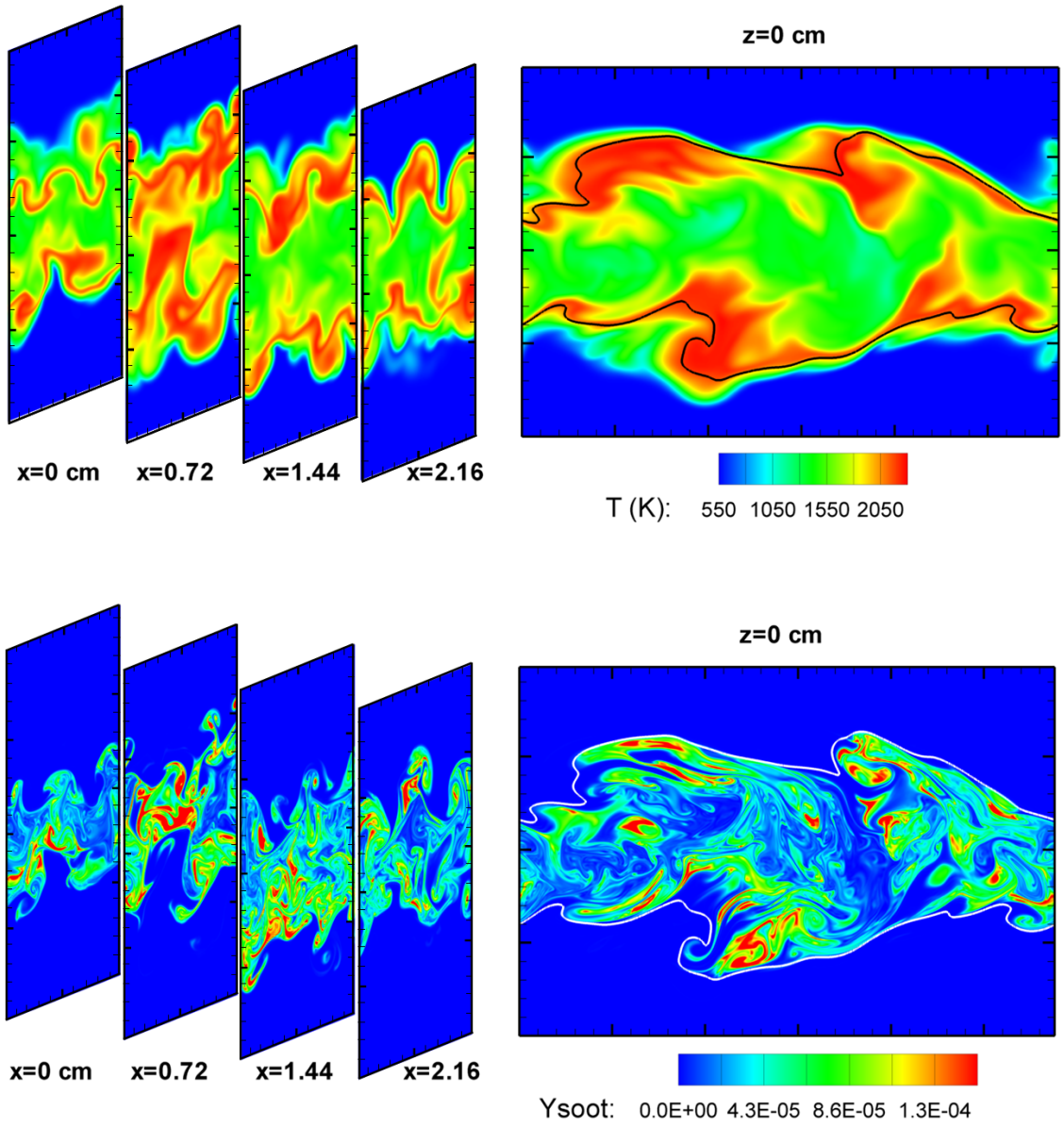

Figure 1: Isocontours of temperature (top) and Y_{soot} (bottom) at $t = 50\tau_j$ for streamwise and spanwise cutting planes. The stoichiometric mixture fraction isocontour is shown in the spanwise cut. The peak Y_{soot} is off scale at 4.5×10^{-4}, located at x=0.72 cm in the central region.

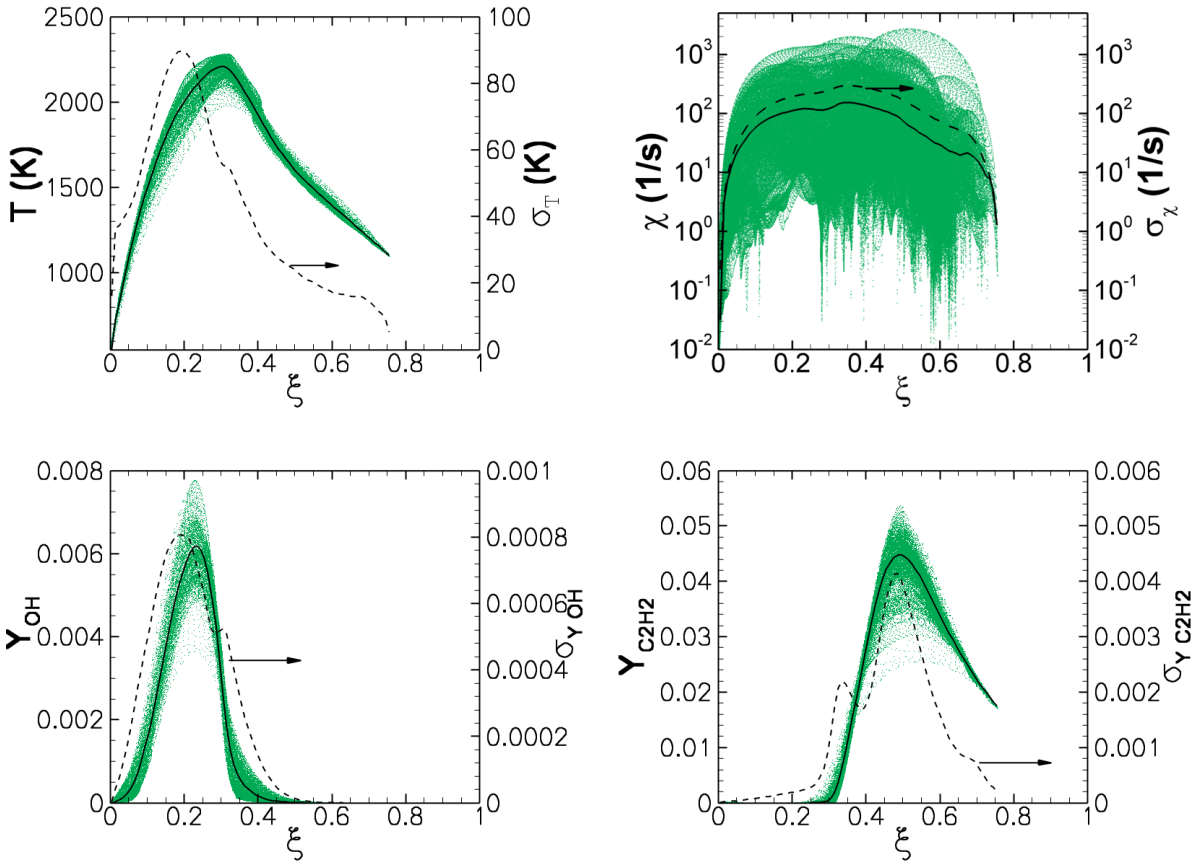

Figure 2: Scatter plots of combustion and flow quantities with conditional means and conditional standard deviations at $t = 50\tau_j$.

those at $t = 50\tau_j$, with the exception that some flame extinction appears in the scatter plots of temperature and OH mass fraction at points significantly below the conditional mean. The conditional mean is not significantly affected by extinction, however, as the extent of the flame extinction is small. The peak flame extinction is 12% at $25\tau_j$. The level of extinction is computed as the fraction of the stoichiometric mixture fraction isosurface with $Y_{OH} < 0.0015$, which is half the steady laminar extinction value.

At $t = 50\tau_j$, the fuel core has mixed out somewhat and the data extends to mixture fractions just below 0.8. The temperature peak occurs rich of the stoichiometric mixture fraction, at $\xi_{st} = 0.3$, whereas the Y_{OH} peak is at a location slightly lean of stoichiometric. This behavior is consistent with one dimensional laminar flame structure. Note that the acetylene concentration peaks at $\xi = 0.5$, which approximately coincides with the peak in χ. This peak will reduce the concentration of soot obtained in the simulation as a higher χ corresponds to a lower residence time for reaction.

The temperature and mass fraction plots in Fig. 2 show a strong state relationship between a given variable and the mixture fraction. This relationship is indicated by values of the standard deviation about an order of magnitude lower than values of the conditional mean.

Figure 3 presents scatter data, conditional means, and conditional standard deviations of the soot moments, and the net chemical source terms of the soot moments. The soot species exhibit distinct behavior from the gaseous species. Note that the conditional scatter in the soot moments is much broader. Hence, the standard deviations of the moments are of the same order of magnitude as the conditional mean. This is in contrast with the gaseous species concentrations, where the conditional standard deviations are an order of magnitude lower than the conditional means. It is widely known that soot moments do not have a simple state relationship with mixture fraction [31]. Here, we observe the same result, which is the source of great difficulty in modeling turbulent sooting flames. In the previous, two dimensional DNS [16], this was shown to be due to the combined effects of unsteady soot growth and strong differential diffusion in the mixture fraction coordinate; the same effects are observed here. Evidence for this is shown by comparing the soot moments to their respective reaction rates. The nucleation rate depends only on gaseous species and has similar characteristics, e.g., a relatively low σ. The rates for the second and third moments, while fixed in the mixture fraction coordinate, show much greater scatter, consistent with their dependence upon the soot moments. Note the crossover from negative to positive reaction rate occurs fuel-rich of ξ_{st} at $\xi = 0.33$ as the soot transitions from being consumed in oxidizing regions, to being formed in growth regions as the mixture fraction is increased. This position is the approximate upper limit in ξ of O_2.

The soot moments span the full range of the mixture fraction domain at mixture fraction values fuel-rich of ξ_{st}, whereas the soot rates vanish at approximately $\xi = 0.6$. The only possible mechanism for this is differential diffusion between soot and mixture fraction, which is the major subject of this paper. This behavior is somewhat masked at $t = 50\tau_j$ since the maximum mixture fraction is below unity. Moreover, due to nitrogen dilution in the fuel core, $\xi_{st} = 0.25$ is much higher than in systems with combustion between pure ethylene and air $\xi_{st} = 0.064$. These two effects render the relative motion between the soot and mixture fraction somewhat obscured as indicated by scatter plots. The relative motion was more readily observed in the earlier two dimensional simulation where there was less mixing of the fuel and oxidizer streams [16]. In the present simulation, at $t = 25\tau_j$, the peak mixture fraction is near unity and the soot moments extend to this upper bound, whereas the soot rates are limited to the regions of mixture fraction shown in Fig. 3.

On the lean side of ξ_{st}, the second two moments are observed to be very small due to the oxidation barrier presented by the flame. The number density (M_0) experiences no such barrier since its only sink is coagulation. For M_0, we observe the extent to which differential diffusion between soot and mixture fraction results in soot transported to lean regions. It is possible that, were the soot mass fraction high enough that oxidation could not fully consume the soot as it is transported past a reactive flame region, substantial quantities of soot could appear at mixture fraction values fuel-lean of ξ_{st}. This process of soot-flame breakthrough, or at least, soot-ξ_{st} breakthrough in the event of flame quenching, may be important in describing soot emissions. In large-scale fires, a substantial quantity of soot is observed to escape the flames where smoke emission occurs along with radiative shielding [32]. Modeling this process is important for performing predictive simulations of heat transfer in and around fires.

3.2.1. Scalar dissipation rate

The scalar dissipation rate is an important quantity in turbulent nonpremixed flames as it determines the rate of mixing between fuel and oxidizer and the combustion heat release rate. The inverse of the scalar dissipation rate is a mixing time scale. In the following presentation, the scalar dissipation rate is directly related to the component of the flame displacement velocity representing diffusion of isosurfaces of mixture fraction in the isosurface-normal direction, relative to convection. Here, statistics of the scalar dissipation rate are first presented.

Figure 4 presents the probability density function (PDF) of $\log_{10}\chi$ at $t = 50\tau_j$. The data are shown on linear and logarithmic scales, and have been centered and normalized to give a mean and standard deviation of zero and unity, respectively. The values of $\langle \log_{10}\chi \rangle$, and $\sigma_{\log_{10}\chi}$ are 1.41, and 0.744, respectively. The data are conditioned on mixture fraction between 0.02 and 0.98 to minimize possible bias associated with the pure streams. The DNS data are shown as symbols and a Gaussian distribution (in $\log_{10}\chi$)

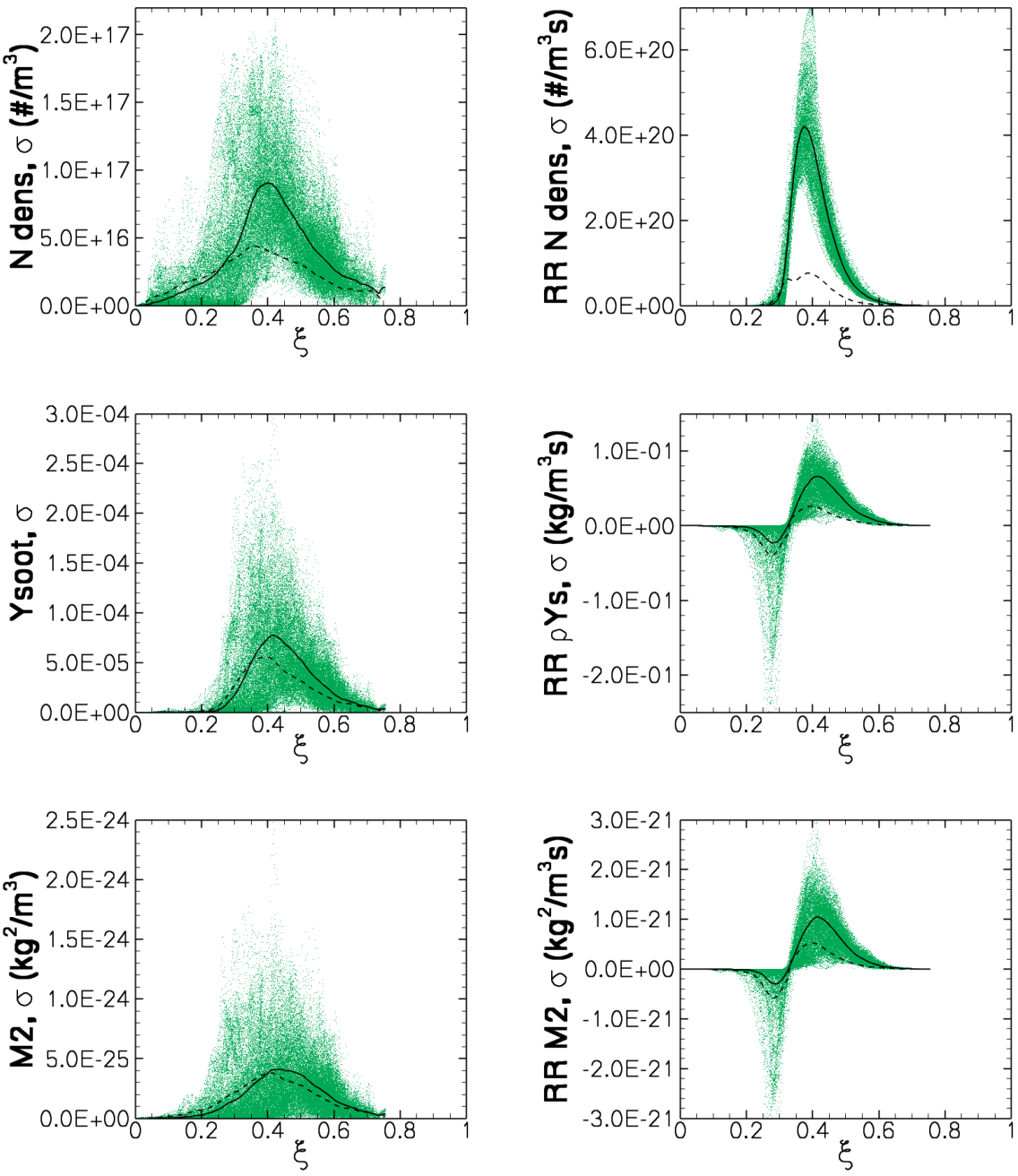

Figure 3: Scatter plots of soot quantities with conditional means (solid) and signed conditional standard deviations (dashed) at $t = 50\tau_j$.

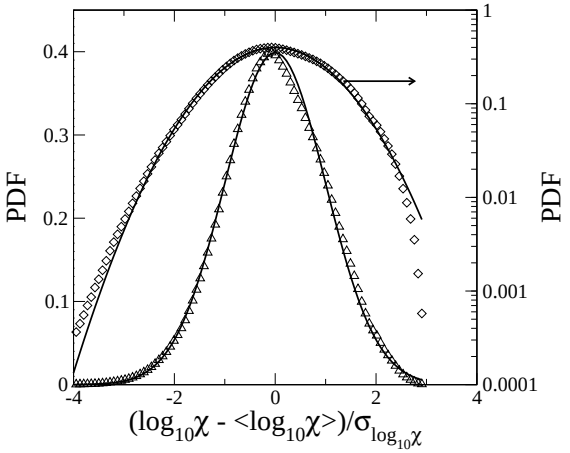

Figure 4: Centered and normalized probability density function of $\log_{10}\chi$ at $t = 50\tau_j$ on linear and log scales. Symbols are data conditioned on $0.02 < \xi < 0.98$. Solid lines are a Gaussian distribution with the same first two moments as the DNS data.

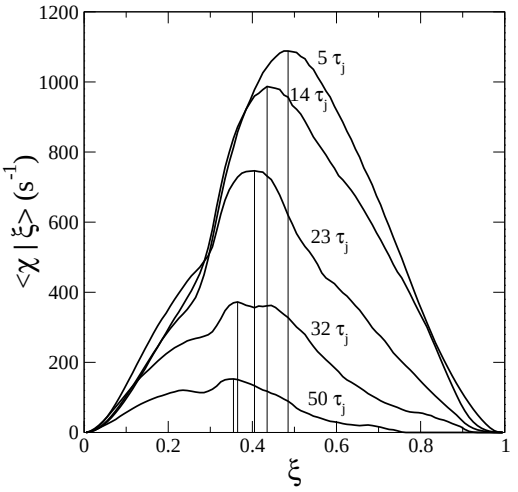

Figure 5: Conditional mean scalar dissipation rate versus mixture fraction at five times. Vertical lines indicate the location of peak conditional scalar dissipation rate.

is shown as the solid line. The Gaussian distribution has the same first two moments as the DNS data. The DNS data are observed to be very nearly lognormal, with a slight negative skewness. These results are in agreement with those previously reported experimentally [27] and in DNS of a similar configuration in an extinction-reignition study of CO-H_2 fuel [33]. While the jet Reynolds number of the present simulation is not large, the turbulence is sufficient to yield a lognormal PDF of the scalar dissipation rate with a wide range of values.

The conditional mean and standard deviation, along with instantaneous scatter data are shown in Fig. 2 for the scalar dissipation rate at $t = 50\tau_j$. Consistent with experimental observations, the standard deviation of the scalar dissipation rate is observed to be higher than the conditional mean value [34]. Though partially obscured by the logarithmic scale, the conditional mean χ has a dip in the vicinity of the stoichiometric point. This has been previously observed experimentally [35], and in DNS [36], and is consistent with effects of flow divergence through gas expansion from the flame, and increased kinematic viscosity (reduced local Re) in the flame zone.

The evolution of the conditional mean scalar dissipation rate is shown in Fig. 5. As the jet evolves, the peak scalar dissipation rate decreases continuously. In addition, as fuel and oxidizer mix, the peak mixture fraction in the fuel core decreases. The mixture fraction value of the peak scalar dissipation rate is indicated in the figure by the vertical lines. The mixture fraction of peak $\langle\chi|\xi\rangle$ becomes progressively lower as the jet evolves. Note at $t = 23\tau_j$ the peak $\langle\chi|\xi\rangle$ occurs at a mixture fraction of approximately 0.4, which coincides with the peak soot mass concentration and reaction rate shown in Fig. 3. At earlier times, the mixture fraction of peak $\langle\chi|\xi\rangle$ is rich of $\xi = 0.4$, and at later times the peak is lean of this value. In a turbulent flow, on average, fluid elements that are rich of the peak $\langle\chi|\xi\rangle$ will become leaner, and fluid elements that are lean of the peak $\langle\chi|\xi\rangle$ will become richer. Hence, as mixture fraction of peak $\langle\chi|\xi\rangle$ crosses $\xi = 0.4$ (where soot production peaks), we expect transport in the mixture fraction coordinate to be non-monotonic, with soot transported to higher, then lower mixture fractions as the jet evolves. This behavior is shown in the following section.

3.3. Mixture Fraction PDF and Soot Transport

The transport of soot in the mixture fraction coordinate is important since this affects the soot concentrations through chemical reactivity, as well as the temperature of the soot, which directly affects radiative emission rates. Figure 6 presents density-weighted (Favre), and soot mass density-weighted, probability density functions of mixture fraction. In Figs. 6a, and 6b, respectively, P_ρ is the fraction of mass per unit mixture fraction at a given mixture fraction, while $P_{\rho Y_s}$ is the fraction of the total soot mass per unit mixture fraction, at a given mixture fraction. These PDFs are defined as

$$P_\phi = \frac{\langle\phi|\xi\rangle P(\xi)}{\langle\phi\rangle}, \tag{2}$$

where ϕ is the weighting variable (ρ, or ρY_s). Fig. 6a has the general shape of a β-PDF. At early times, the mixture fraction is partitioned mainly between pure fuel and oxidizer (mostly oxidizer). As the jet evolves, the fuel stream mixes out and the upper bound migrates towards leaner mixture fraction. At $t = 50\tau_j$, the peak mixture fraction is just below 0.8, and the peak in the PDF is just

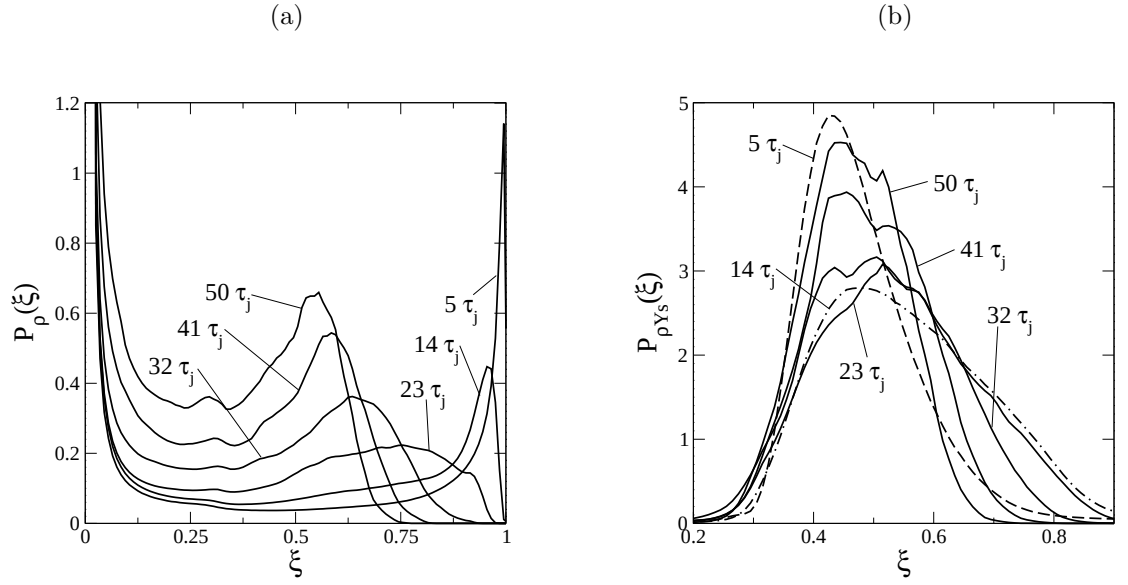

Figure 6: Density-weighted, (a), and soot mass density-weighted, (b), probability density functions of mixture fraction at evenly spaced times.

above 0.5, which corresponds with the location of the peak acetylene mass fraction, shown in Fig. 2.

Figure 6b is more interesting; it has an approximate Gaussian shape, but with a noticeable positive skewness, i.e., a tail towards the fuel stream. As the jet evolves, the probability density function first widens, and subsequently contracts. This is a consequence of two competing effects:

1. Differential diffusion between soot and mixture fraction, as evidenced by the soot locality outside of the mixture fraction bounds of the soot reaction rates (see Fig. 3). This differential diffusion occurs due to the dynamics between mixing of soot and isocontours of mixture fraction.
2. As fuel and oxidizer mix together, the fuel core is diluted and the upper bound of mixture fraction decreases in time.

Hence, while differential diffusion of soot and mixture fraction tends to spread soot in the mixture fraction coordinate, the upper bound on the mixture fraction is becoming smaller as gas mixing occurs. Time in the present simulation is the analogue of axial position in a nonpremixed jet flame. If the present simulation were continued to longer time, we would expect the peak in the mixture fraction PDF to approach the stoichiometric value and eventually mix to the oxidizer free-stream composition. The soot would be squeezed towards the flame zone until soot oxidation (and possibly some emission) occurs.

Soot is essentially convected with the fluid, and the rate of motion of isocontours of mixture fraction relative to fluid convection gives the motion of soot with respect to mixture fraction. This motion can be of either positive or negative sign, as was previously demonstrated in two dimensional simulation [16] by examining the so-called

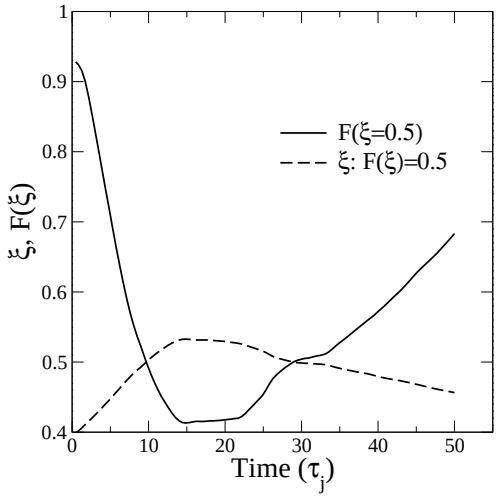

Figure 7: Plot of the cumulative soot mass density-weighted probability density function of mixture fraction evaluated at $\xi = 0.5$ (solid). The dashed line shows the mixture fraction location where the same cumulative probability density function has a value of 0.5.

flame displacement velocity v_ξ. This quantity is elaborated on below for the present three dimensional simulation. Unlike the present case, in the two dimensional DNS the peak mixture fraction did not decrease substantially below unity, and bulk mixing of the fuel zone was not observed.

Figure 7 highlights the location and width of $P_{\rho Y_s}$ in ξ that was presented in Fig. 6. Here we consider the

cumulative soot mass-weighted PDF of mixture fraction:

$$F(\xi) = \int_0^{\xi} P_{\rho Y_s}(\xi')d\xi', \tag{3}$$

where ξ' is an integration variable for ξ. The solid line in Fig. 7 is the value of $F(\xi = 0.5)$ and is the fraction of the total soot mass below a mixture fraction of 0.5. This value starts at over 90% and decreases to below 50% as the soot is transported towards richer ξ. The curve then reaches its minimum point just above 40% at $14\tau_j$. At approximately $23\tau_j$, the curve rises sharply and increases to approximately 70% at $50\tau_j$ as the fuel stream is mixed out and the peak mixture fraction decreases. Recall from Fig. 5 that $23\tau_j$ corresponds to the time at which the peak $\langle\chi|\xi\rangle$ crosses $\xi = 0.4$, which is where the conditional mean soot mass and soot mass rate exhibit maxima.

The dashed curve in Fig. 7 indicates the motion of $P_{\rho Y_s}$. This curve represents the location in the mixture fraction coordinate of the median soot mass. The dashed curve is qualitatively the inverse of $F(\xi = 0.5)$ and shows that the location of the median soot mass starts out lean at a mixture fraction of about $\xi = 0.4$. The mixture fraction at $F(\xi) = 0.5$ then increases in time to $\xi = 0.53$, where it peaks at about the same time as the minimum in $F(\xi = 0.5)$, after which it decreases monotonically to $\xi = 0.45$.

3.4. Mixture Fraction Dynamics and Soot-Flame Diffusion

As soot is primarily convected with the fluid, the differential diffusion between the soot and mixture fraction can be quantified using the velocity of isocontours of the mixture fraction relative to the convective velocity. This velocity occurs via diffusion of isoscalar surfaces in the direction normal to the surface, as derived by Gibson [37], and Pope [38]. For variable property flow, we have

$$\boldsymbol{v_\xi} = -\frac{\nabla \cdot (\rho D_\xi \nabla \xi)}{\rho |\nabla \xi|}\mathbf{n}. \tag{4}$$

The flame displacement velocity, v_ξ, is evaluated at ξ_{st}, where ρ is density, and D_ξ is mixture fraction diffusivity obtained assuming a unity Lewis number. The unit surface normal is defined as $\mathbf{n} = \frac{\nabla \xi}{|\nabla \xi|}$, where the positive normal points towards the fuel stream. Following Echekki and Chen [39], this velocity can be expanded in terms of the flame normal coordinate into two terms:

$$v_\xi = -D_\xi \nabla \cdot \mathbf{n} - \frac{1}{\rho|\nabla\xi|}\frac{\partial}{\partial \eta}\left(\rho D_\xi \frac{\partial \xi}{\partial \eta}\right) \tag{5}$$

$$= -D_\xi \nabla \cdot \mathbf{n} - \frac{D_\xi}{2}\frac{\partial}{\partial \eta}\ln\left(\rho^2 D_\xi \chi/2\right). \tag{6}$$

Here, η is the flame-normal coordinate in the direction $\mathbf{n}$. The first term in the equation is a curvature term, where $\nabla \cdot \mathbf{n}$ is the mean surface curvature, and is negative when the center of curvature is in the fuel stream. A negative curvature contributes to v_ξ moving towards the fuel stream, and vice versa. The second term is relative flame motion arising from diffusion in the flame-normal direction. This term is rewritten in terms of the scalar dissipation rate in Eq. (6).

Equations (5) and (6) describe the fine-scale velocity of isocontours of the mixture fraction relative to convection. The equations hold for all values of mixture fraction, although the stoichiometric value is the focus of attention in this paper. These equations will hold in both two- and three dimensional turbulence and their constitutive components, that is, curvature and normal diffusion or strain are present in both two- and three dimensional turbulent flows. As a result, similarities are expected in the qualitative behavior of the flame displacement velocity regarding relative soot transport. Although the strain and curvature features are common to two- and three dimensional turbulence, three dimensional turbulence is fundamentally different in that it supports vortex stretching and a turbulent energy cascade, resulting in enhanced mixing rates. The qualitative differences between two- and three dimensional turbulence may shift the relative importance and signs of the terms in the referenced equations.

In the two dimensional analysis, it was found that the curvature term has either sign with a mean near zero, while the normal diffusion term is primarily negative since the flame exists between pure streams at a low value of the mixture fraction, such that a diffusive relaxation of the flame tends to move the flame towards the oxidizer stream. In other words, the second derivative of the mixture fraction profile in the η coordinate was almost exclusively positive. This behavior is dependent on the stoichiometric value of the mixture fraction and may be reversed if the fuel stream is diluted to the point where the stoichiometric mixture fraction is very high. Here, $\xi_{st} = 0.25$ is much higher than $\xi_{st} = 0.064$ for pure ethylene-air streams, hence closer to the nominal inflection point in the ξ profile, which varies smoothly in an S-shape between the pure streams. This, together with the decreasing upper bound on ξ, through bulk fuel-oxidizer mixing, results in the normal diffusion term taking on both positive and negative values, as shown below.

Figure 8 presents the stoichiometric isosurface colored by v_ξ at six times along with grayscale isocontours of the soot mass fraction. Note that the scales vary with time. At early times, there is a strong positive correlation between the soot concentration and the magnitude and sign of v_ξ. Regions of positive v_ξ correspond to the flame moving towards the fuel stream relative to convection. In these regions, the soot is locally convected towards the flame zone where its temperature is higher and the soot is more reactive. This behavior was observed in the two dimensional simulation [16]. There, the turbulence was decaying, the Reynolds number was smaller, and the soot was not strongly convected away from the flame zone. Here, at $14\tau_j$, spanwise coherent structures associated with the Kelvin-Helmholtz shear instability are evident, which convectively transport soot away from the flame zone. These

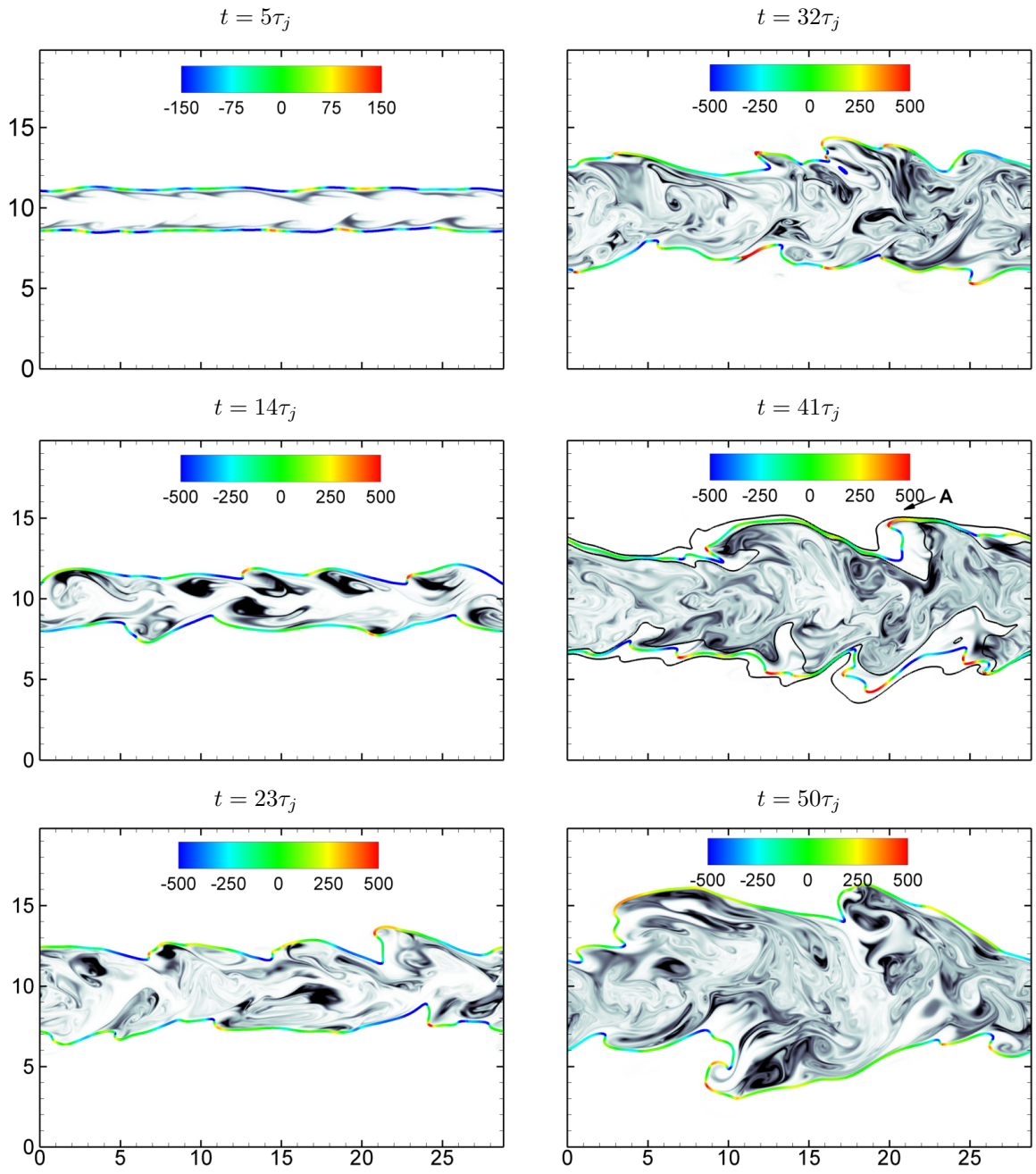

Figure 8: Y_{soot} (grayscale, black is high value) and stoichiometric isosurface colored by v_ξ. The scales vary: with increasing time the peak Y_{soot} scale is 1×10^{-5}, 1×10^{-5}, 4×10^{-5}, 5×10^{-5} 10×10^{-5}, 15×10^{-5}. The length dimension is mm. At $41\tau_j$ two additional mixture fraction isocontours , 0.15 and 0.35 are shown.

strong transport and history effects complicate the analysis and preclude a simple monotonic increase of mixture fraction across the flame from pure air to pure fuel. Ideally, a Lagrangian description of the soot would record the full history, especially the reactive history, of the soot. As it is, soot is formed and grows in reactive zones near the flame. Subsequently, turbulence transports the soot away from the flame where mixing increases the local mixture fraction surrounding the soot, hence reducing the soot temperature and growth rate, but soot remains to be strained and diluted by the flow. The soot structures persist even as the turbulent energy decays, serving as an example of Gibson's so-called fossil turbulence [40].

At later times, e.g., $t = 41\tau_j$, there are regions of high v_ξ for which the soot concentration appears to be very small. There are two possible reasons for this. One is simply that the thickness of the colored stoichiometric surface obscures a high concentration of soot beneath it. This occurs, for example, at $t = 41\tau_j$ on the right of the upper flame sheet at point "A". More importantly, the flame sheet is wrinkled with a curvature that changes sign, and hence, can change the sign of v_ξ. Therefore, soot may be formed preferentially in a region of positive v_ξ, which subsequently changes sign through flame curvature, but leaves a higher concentration of soot in its wake.

At $t = 41\tau_j$, mixture fraction isocontours at 0.15 and 0.35 are also shown. Note that in some regions, soot appears to be absent "far" from the flame, but that these regions, in fact, coincide with the spacing of the mixture fraction contours. That is, the soot is not "far" from the flame in the mixture fraction coordinate, since extensive strain rate in the upstream portions of the spanwise rollers separates the mixture fraction isocontours. From Fig. 3, the crossover between production and destruction of $M_1 = \rho Y_s$ occurs at $\xi = 0.33$, which accounts for the low soot mass between these isocontours.

3.5. The Flame Displacement Velocity and Its Terms

The stoichiometric mixture fraction probability density functions of v_ξ and its constituent terms at three times corresponding to $5\tau_j$, $23\tau_j$ and $41\tau_j$ are presented in Fig. 9. In the figure, CRV and ND denote the curvature and normal diffusion terms, respectively, on the right-hand-side of Eq. (5). These probability density functions are area-weighted on the stoichiometric surface extracted from the mixture fraction field. The scale of the terms in the figure indicates that both terms of v_ξ are of similar magnitudes. It is also observed that the terms are of either positive or negative sign, although the normal diffusion term and v_ξ are negatively biased. Recall that positive values of the curvature term, normal diffusion term, and v_ξ correspond to convection through the flame from the fuel side to the oxidizer side, or, relative to convection, positive values of these terms correspond to diffusion of the ξ_{st} isosurface towards the fuel stream. The converse is true for negative values of these quantities.

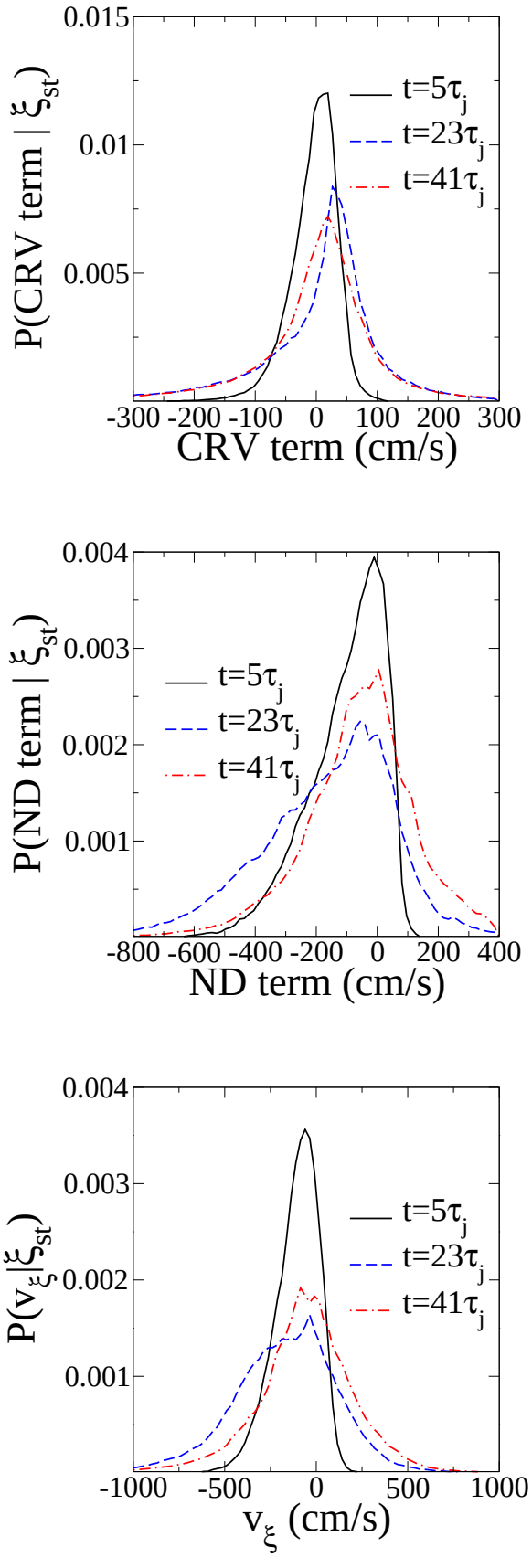

Figure 9: Probability density functions of v_ξ, Eq. (4), and its two terms Eq. (5), conditioned on ξ_{st} at three times.

The normal diffusion term is observed from Fig. 9 to have a negative skewness. As noted previously, in the absence of curvature, in an ideal diffusion flame with $\xi_{st} \lesssim 0.5$, the mixture fraction profile through the flame will have a positive second derivative for which diffusive relaxation will move the flame towards the oxidizer. This effect is less strong as ξ_{st} increases towards the inflection point (at which point the sign changes and the diffusive relaxation causes flame motion towards the fuel side). Conversely, as the jet evolves, the maximum mixture fraction decays due to mixing, and the inflection point in the mixture fraction profile moves towards the stoichiometric surface. This results in an increased portion of the flame existing with a positive normal diffusion term, hence a more positive v_ξ. The effect of the terms on the stoichiometric probability density function of v_ξ is also shown in Fig. 9. v_ξ is always biased to negative values, as expected due to the small mean of the curvature term and the negative bias of the normal diffusion term. As the jet evolves, however, this bias is reduced and the fraction of positive v_ξ increases from 22.8% at $5\tau_j$ to 49.1% at $50\tau_j$. Table 3 shows the fraction of the stoichiometric surface for which the curvature term, normal diffusion term, and v_ξ are positive at six times in the simulation. The fraction of positive curvature term shows little variation, while the fraction of positive normal diffusion term and v_ξ have similar values and steadily increase in time.

The fact that v_ξ is significantly positive is important from a modeling perspective because it means that multidimensional effects associated with flame curvature, and mixing effects associated with normal diffusion can result in a diffusion flame that moves (relative to convection) in both the fuel and oxidizer directions with nearly equal frequency. Positive v_ξ is the opposite of what occurs in canonical opposed jet diffusion flames of similar stream compositions. While these effects may play a small role in the combustion gas dynamics, they are shown to play a strong role in soot formation and radiative processes in the two dimensional simulations [16]. Here, it is demonstrated that similar flame dynamics are observed in both two- and three dimensional turbulence.

Figure 10 presents the area-weighted stoichiometric mean and standard deviation of v_ξ, and the curvature and normal diffusion terms, as a function of time. Note that the mean curvature term is nearly zero, but its standard deviation is significant. The difference between the mean v_ξ and mean normal diffusion term is the mean curvature term, which is small. Hence, the mean v_ξ closely follows the mean normal diffusion term. The mean v_ξ and normal diffusion terms are negative for the extent of the simulation, up to $50\tau_j$. However, the mean normal diffusion term at first decreases to a minimum of -200 cm/s at $16\tau_j$, but then increases steadily to -14 cm/s at $50\tau_j$. The minimum curvature term is -10 cm/s at 23 τ_j.

The standard deviation of the normal diffusion term is approximately twice that of the curvature term in the first quarter of the simulation, after which the discrepancy in the standard deviations becomes smaller. The standard deviation of the normal diffusion term is comparable to its mean value over the first half of the simulation. The combination of the location of the mean and the magnitude of the standard deviation indicates the extent to which the curvature and normal diffusion terms contribute to positive and negative v_ξ.

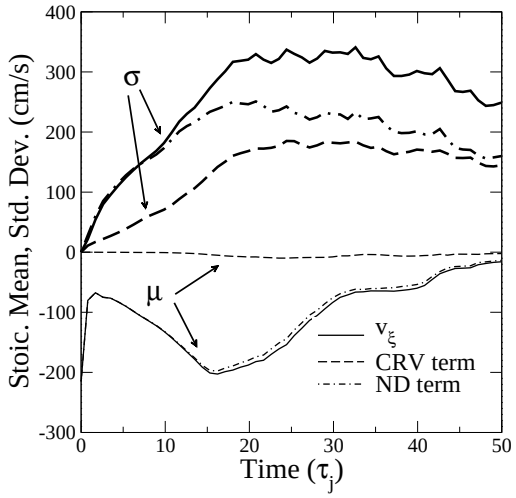

Figure 10: Stoichiometric conditional means, μ, (thin) and conditional standard deviations, σ, (bold) of v_ξ and its constituent terms.

More detailed insight into the relationship between the various terms considered is obtained from the correlation coefficient. The stoichiometric correlation coefficient between pairs of terms is shown in Fig. 11. The correlation coefficient is defined as

$$\varrho_{X,Y} = \frac{\langle XY \rangle - \langle X \rangle \langle Y \rangle}{\sigma_X \sigma_Y}, \tag{7}$$

where, X and Y denote the variables of the correlation. The correlation between v_ξ and the normal diffusion term is strongly positive, having a value above 0.83 throughout the simulation, as the diffusive velocity of the stoichiometric mixture fraction isosurface is directly influenced by turbulent straining in the flame-normal direction. The correlation coefficient of v_ξ and the curvature term is not as large as for v_ξ and the normal diffusion term. A positive correlation for v_ξ and the curvature corresponds to the flame moving (relative to convection) towards the fuel stream when the center of curvature is in the fuel stream. The correlation is initially negative as the jet develops, then increases continuously throughout the simulation. This rise in $\varrho_{v_\xi, CRV}$ is consistent with the increasing importance of the curvature term to v_ξ, compared with the normal diffusion term, indicated by comparing their means and standard deviations in Fig. 10. Except for an initial transient, the magnitude of the correlation coefficient between the curvature and normal diffusion terms directly is less than 0.33 throughout the simulation. The values

Table 3: Positive fraction of stoichiometric surface quantities.

Time (τ_j)	v_ξ	Curvature Term	Normal Diffusion Term
5	0.228	0.558	0.254
14	0.235	0.632	0.228
23	0.291	0.636	0.248
32	0.412	0.594	0.395
41	0.427	0.588	0.402
50	0.491	0.580	0.492

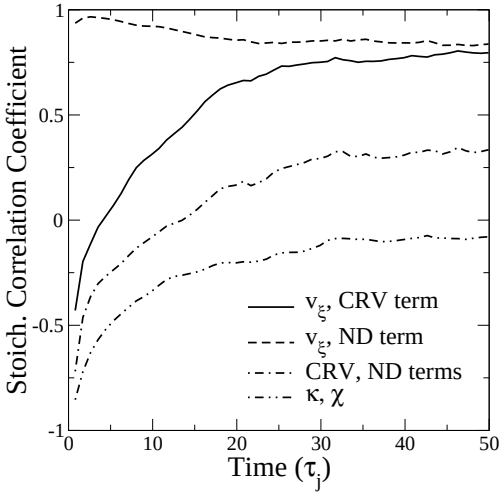

Figure 11: Stoichiometric correlation coefficient between various terms as a function of time.

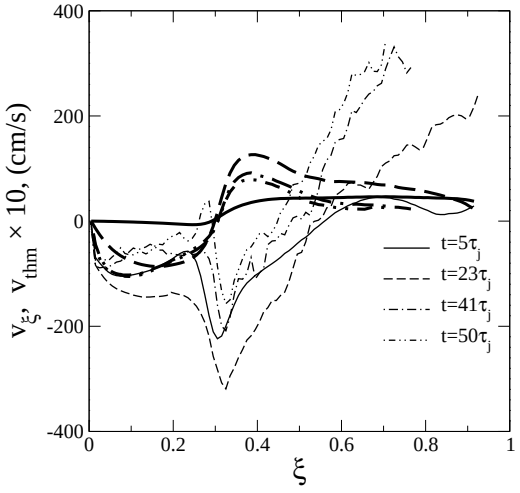

Figure 12: Conditional mean thermophoretic velocity (bold), and mixture fraction displacement velocity (thin) at four times.

of $\varrho_{v_\xi,CRV}$ and $\varrho_{v_\xi,ND}$ are higher than $\varrho_{CRV,ND}$ because the former two quantities include the correlation of the curvature and normal diffusion terms with themselves.

As noted, the mean curvature term in v_ξ is slightly negative throughout the simulation. However, the mean curvature, κ, of the stoichiometric surface is nearly zero. The curvature term is the product of the curvature and D_ξ. The difference between the curvature and the curvature term is due to the temperature dependence of D_ξ (as temperature increases D_ξ increases), and the location of ξ_{st}. When the flame has a negative curvature, χ_{st} tends to be higher than when the flame has a positive curvature, as shown in Fig. 11. These higher χ_{st} with negative curvature κ result in a lower flame temperature, and a lower D_ξ, hence a lower curvature term. The χ-κ relation at ξ_{st} results from the bias towards extensive strain of $\xi \lesssim 0.5\xi_{max}$ with negative curvature. The correlation coefficient between κ and χ on the stoichiometric mixture fraction surface increases from -0.5 at $5\tau_j$, to -0.08 at $50\tau_j$. Initially, the stoichiometric mixture fraction is 0.25, and the peak mixture fraction is unity. At $50\tau_j$, the peak in the mixture fraction PDF occurs at $\xi = 0.5$. The peak in $\langle\chi|\xi\rangle$ occurs at $\xi = 0.5$ and $\xi = 0.35$ at $t = 0$ and $t = 50\tau_j$, respectively. Hence, the magnitude of the correlation coefficient between curvature and scalar dissipation rate decreases as the position of the peak of $\langle\chi|\xi\rangle$ approaches the the stoichiometric mixture fraction.

3.6. Thermophoretic Diffusion Velocity

The conditional mean thermophoretic diffusion velocity $\langle v_T|\xi\rangle$, and flame displacement velocity $\langle v_\xi$ at four times, are presented in Fig. 12. Here, v_ξ refers to the velocity at a given mixture fraction, and not the stoichiometric surface. Note that the scale of $\langle v_T|\xi\rangle$ is a factor of ten lower than the scale of $\langle v_\xi|\xi\rangle$, while the curves are of similar magnitude on the scale given. Hence, the thermophoretic velocity is much smaller than the differential diffusion velocity between the gas and the soot fields. The relatively low thermophoretic diffusion velocity reinforces the presumption that soot is essentially convected with the flow field, and that soot-mixture fraction transport may be quantified using v_ξ.

The curves of conditional mean v_ξ cross from negative to positive value close to $\xi = 0.5$ at the times shown.

Hence, isocontours of mixture fraction above $\xi \approx 0.5$ are moving towards the fuel stream, or in other words, towards the jet center, and isocontours of mixture fraction below $\xi \approx 0.5$ are moving towards the oxidizer stream as the jet spreads. As the jet evolves and mixing occurs, the crossover mixture fraction shifts towards smaller mixture fraction. In the negative v_ξ regions, the magnitude of v_ξ first increases, then decreases in time, whereas the magnitude of the positive regions increases with time. The value of v_ξ approaches zero as ξ approaches zero, that is, as the free oxidizer stream is approached. At the upper bound of ξ, the velocity is positive as the highest ξ isocontours move towards the jet center region, then merge, and are annihilated as oxidizer mixes into the core.

4. Discussion

The present simulation provides not only insight into soot formation and transport processes, but a database by which models of turbulent soot formation may be developed and quantitatively validated.

The unsteady growth of soot that overlaps convective and diffusive time scales, and the transport of soot in the mixture fraction coordinate, are difficult problems in modeling soot formation in turbulent flames. The conditional moment closure (CMC) model solves unsteady transport equations for reactive scalars conditionally averaged on the mixture fraction [41]. CMC formulations have been developed that allow for differential diffusion of reactive scalars [42, 41, 43], and CMC modeling of turbulent sooting flames has been successfully applied [44]. In CMC, accurate modeling of transport of conditionally averaged scalars in the mixture fraction coordinate is important. In the conservation-form of the CMC formulation of Hewson et al. [43], the quantity $|\nabla\xi|v_\xi$ appears directly in the differential diffusion term of the conditional mean transport equation for the soot moments. Here, $|\nabla\xi|v_\xi$ has units of inverse seconds, or *mixture fraction* per second, and represents a diffusion velocity in the mixture fraction coordinate. Hence, the relative mixture fraction displacement velocity v_ξ has direct relevance to practical models of turbulent soot formation. The evaluation of combustion models, such as the CMC model, will be the focus of future work.

This simulation represents a first step towards providing a detailed view of soot formation and transport in a turbulent flow, and as such, several concessions were made to limit computational costs. The present soot model does not account for the role of PAH and radical species (such as H) in the nucleation, growth and oxidation processes. Quantitative detailed soot models are the subject of ongoing research. The effect of detailed soot chemistry will impact the location of the soot reactivity within the flame zone. The role of hydrogen in the soot growth process may be important as hydrogen exhibits strong differential diffusion with respect to other gaseous species. The details of the soot chemistry may alter the quantitative soot concentrations. However, the primary results presented here on the flame dynamics and soot-flame interaction with soot transport occurring over the full range of ξ are not expected to be sensitive to the details of the soot model employed.

In order to resolve the time and length scales of the simulation with a fixed computational cost, the simulation time was limited to 1.1 ms. This relatively short duration, combined with the relatively high velocity of the jet and the increased stoichiometric mixture fraction, result in lower soot concentrations. The peak soot concentration observed in the present simulation is $f_{v,peak} = 0.03$, which is comparable to experimental values in methane flames [45]. In larger-scale configurations (e.g., fires), longer residence times occur for soot growth and radiative heat transfer, with significantly stronger soot-flame interactions expected. However, the basic interactions between soot and the flame due to differential transport influenced by the flame dynamics are expected to remain.

The present simulation describes the early-to-intermediate stages of the jet development and mixing. Near the end of the simulation, the (rich) peak of the mixture fraction PDF has mixed towards lower ξ and overlaps with the peak of the conditional mean soot mass fraction. In the process, the soot is being forced towards leaner mixture fraction, where oxidation will eventually occur. An important extension to the present work is the simulation of the latter portion of the jet mixing in which soot is transported fully into the flame and burned out. Computational costs to reach this state from a developing jet as performed here are currently prohibitive. However, an initial condition could be constructed such that the entirety of the resultant jet development proceeds in the desired regime of jet mixing (e.g., from the desired intermediate jet composition and Reynolds number). The effect of soot concentration could be studied by seeding the flow with higher concentrations of soot, allowing substantial soot-flame interactions and possible soot emission.

5. Conclusions

three dimensional DNS of a turbulent ethylene jet flame has been performed with realistic chemistry and transport. The simulation includes soot formation using a standard model and represents the first DNS of soot formation in a three dimensional turbulent flame with realistic gas-phase combustion chemistry. The previous two dimensional decaying turbulence simulation provided detailed insight into soot-flame interactions, but the quantity of data available was relatively small for statistical representation. In addition, one may question the applicability of results based on two dimensional turbulence.

The turbulent flow field of the three dimensional simulation is substantially more complex than the two dimensional simulation due to enhanced mixing rates associated with turbulence generation by vortex stretching and the

generation of small-scale flow structures. However, analysis of soot flame interactions and soot transport in terms of the velocity of mixture fraction isocontours remains valid. Similarities between the two- and three dimensional configuration are expected on the basis that the strain and curvature components of the mixture fraction velocity are common to both flow types. However, the magnitude, sign and statistical distribution of the these terms of the mixture fraction velocity depend on the turbulent flow investigated. This paper has quantified the mixture fraction velocity and its constitutive terms in the context of soot formation and transport in an idealized, but physically relevant turbulent flow configuration.

Important results of the present simulation are summarized below:

- The turbulent flame yields a lognormal probability density function of scalar dissipation rate with a negative skewness in agreement with nonreacting experimental data and reacting DNS results.
- Motion of soot in the mixture fraction coordinate arises from differential diffusion between soot and mixture fraction, as well as the bulk effect of mixing of the fuel jet core. The location of soot in the mixture fraction coordinate has previously been shown to directly impact the temperature and gas composition that the soot experiences, and hence its radiative heat transfer and reaction rates [16].
- To quantify the differential diffusion between the gas and the soot, the diffusive velocity of mixture fraction isocontours relative to convection, v_ξ, is computed at the flame surface. A positive value of v_ξ results in motion of the ξ surface towards the fuel stream (and vice versa). The curvature and normal diffusion terms of v_ξ are computed and found to be of similar magnitude and of either sign. As the jet evolves, the curvature PDF remains centered at zero, while the positive fraction of the normal diffusion term progressively increases, resulting in an increase in the fraction of positive v_ξ.
- A substantial portion of the ξ_{st} surface (nearly 50% towards the end of the simulation) has $v_\xi > 0$. In these regions soot is convected towards the flame, which is the opposite of what occurs in canonical opposed jet/flamelet configurations commonly used in modeling.
- The thermophoretic velocity is found to be lower than v_ξ by an order of magnitude over the range of ξ, indicating that thermophoretic effects are small compared to differential diffusion effects between gaseous species and soot.

Results in common between the present simulation and the previous two dimensional decaying turbulence simulation include: (1) the correlation between the flame displacement velocity and the soot concentration; (2) the importance of both terms of the flame displacement velocity and the presence of either sign for the terms; and (3) the dominance of this velocity over the thermophoretic diffusion velocity of soot.

Notable differences in the present simulation over the two dimensional simulations include: (1) enhanced turbulent mixing between the free streams and a more complex flow structure that remains active throughout the simulation; (2) a competition between turbulent soot transport towards higher mixture fractions and the reduction in the peak mixture fraction through substantial bulk mixing of the fuel and oxidizer streams; and (3) the positive shift in the PDF of the normal diffusion term of the flame displacement velocity with time resulting in a substantial positive fraction of that term and the flame displacement velocity.

6. Acknowledgments

This work was supported by the U. S. Department of Energy, Office of Basic Energy Sciences, Division of Chemical Sciences, Geosciences, and Biosciences. Simulations were performed at Sandia National Laboratories on the Redstorm supercomputer. Sandia National Laboratories is a multiprogram laboratory operated by Sandia Corporation, a Lockheed Martin Company, for the United States Department of Energy under contract DE-AC04-94-AL85000.

References

[1] H. Bockhorn. *Soot formation in combustion.* Springer-Verlag, Heidelberg, Germany, 1994.

[2] M. Frenklach and H. Wang. Detailed mechanism and modeling of soot particle formation. In H. Bockhorn, editor, *Soot Formation in Combustion*, pages 165–196. Springer-Verlag, New York, 1994.

[3] B. Zhao, Z. Yang, J. Wang, M. V. Johnston, and H. Wang. Analysis of soot nanoparticles in a laminar premixed ethylene flame by scanning mobility particle sizer. *Aerosol. Sci. Tech.*, 37:611–620, 2003.

[4] M. D. Smooke, R. J. Hall, M. B. Colket, J. Fielding, M. B. Long, C. S. McEnally, and L. D. Pfefferle. Investigation of the transition from lightly sooting towards heavily sooting co-flow ethylene diffusion flames. *Combust. Theor. Model.*, 8:593–606, 2004.

[5] T. Steinhaus, S. Welch, R. O. Carvel, and J. L. Torero. Large-scale pool fires. *Thermal Science*, 11:101–118, 2007.

[6] S. K. Friedlander. *Smoke Dust and Haze: Fundamentals of Aerosol Behavior.* John Wiley and Sons, New York, first edition, 1977.

[7] H. Pitsch, E. Riesmeier, and N. Peters. Unsteady flamelet modelling of soot formation in turbulent diffusion flames. *Combust. Sci. Technol.*, 158:389–406, 2000.

[8] B. S. Haynes and H. G. Wagner. Soot formation. *Prog. Energy Combust. Sci.*, 7(4):229–273, 1981.

[9] K. J. Young and J. B. Moss. Modelling sooting turbulent jet flames using an extended flamelet technique. *Combust. Sci. Technol.*, 105:33–53, 1995.

[10] K. M. Leung and R. P. Lindstedt. A simplified reaction mechanism for soot formation in nonpremixed flames. *Combust. Flame*, 87:289–305, 1991.

[11] N. J. Brown, K. L. Revzan, and M. Frenklach. Detailed kinetic modelling of soot formation in ethylene-air mixtures reacting in a perfectly stirred reactor. *Proc. Combust. Inst.*, 27:1573–1580, 1962.

[12] C. R. Shaddix, T. C. Williams, L. G. Blevins, and R. W. Schefer. Flame structure of steady and pulsed sooting inverse jet diffusion flames. *Proc. Combust. Inst.*, 30:1501–1508, 2005.

[13] M. A. Mikofski, T. C. Williams, C. R. Shaddix, A. C. Fernandez-Pello, and L. G. Blevins. Structure of laminar sooting inverse diffusion flames. *Combust. Flame*, 149:463–478, 2007.

[14] P. E. Desjardin and S. H. Frankel. two dimensional large eddy simulation of soot formation in the near-field of a strongly radiating nonpremixed acetylene-air turbulent jet flame. *Combust. Flame*, 119:121–132, 1999.

[15] C. S. Yoo and H. G. Im. Transient soot dynamics in turbulent nonpremixed ethylene-air counterflow flames. *Proc. Combust. Inst.*, 31:701–708, 2006.

[16] D. O. Lignell, J. H. Chen, P. J. Smith, T. Lu, and C. K. Law. The effect of flame structure on soot formation and transport in turbulent nonpremixed flames using direct numerical simulation. *Combust. Flame*, 151(1-2):2–28, 2007.

[17] Y. Ju, H. Guo, K. Maruta, F. Liu, On the extinction limit and flammability limit of non-adiabatic stretched methaneair premixed flames, J. Fluid Mech. 342 (1997) 315–334.

[18] C. A. Kennedy, M. H. Carpenter, and R. M. Lewis. Low-storage, explicit runge-kutta schemes for the compressible navier-stokes equations. *Appl. Num. Math.*, 35(3):177–219, 2000.

[19] C. A. Kennedy and M. H. Carpenter. A comparison of several new numerical methods for the simulation of compressible shear layers. *Appl. Num. Math.*, 14(4):397–433, 1994.

[20] R. J. Kee, F. M. Rupley, and J. A. Miller. *Chemkin.* Reaction Design, Inc., San Diego CA, 2000.

[21] R. J. Kee, G. Dixon-Lewis, J. Warnatz, M. E. Coltrin, J. A. Miller, and H. K. Moffat. *Transport.* Reaction Design, Inc., San Diego CA, 2000.

[22] Z. Qin, V. V. Lissianski, H. Yang, W. C. Gardiner, S. G. Davis, and H. Wang. Combustion chemistry of propane: a case study of detailed reaction mechanism optimization. *Proc. Combust. Inst.*, 28:1663–1669, 2000.

[23] J.Appel, H. Bockhorn, and M. Frenklach. Kinetic modelling of soot formation with detailed chemistry and physics: laminar premixed flames of C_2 hydrocarbons. *Combust. Flame*, 121:122–136, 2000.

[24] S. E. Pratsinis. Simultaneous nucleation, condensation, and coagulation in aerosol reactors. *J. Colloid. Interf. Sci.*, 124(2):416–427, 1987.

[25] R. McGraw. Description of aerosol dynamics by the quadrature method of moments. *Aerosol. Sci. Tech.*, 25:255–265, 1997.

[26] J. C. Sutherland and C. A. Kennedy. Improved boundary conditions for viscous reacting compressible flows. *J. Comput. Phys.*, 191:502–524, 2003.

[27] L. K. Su and N. T. Clemens. The structure of fine-scale scalar mixing in gas-phase planar turbulent jets. *J. Fluid Mech.*, 488:1–29, 2003.

[28] T. Passot and A. Pouquet. Numerical simulation of compressible homogeneous flows in the turbulent regime. *J. Fluid Mech.*, 181:441–466, 1987.

[29] J. Du and R. L. Axelbaum. The effect of flame structure on soot-particle inception in diffusion flames. *Combust. Flame*, 100:367–375, 1995.

[30] R. W. Bilger, S. H. Starner, and R. J. Kee. On reduced mechanisms for methane-air combustion in nonpremixed flames. *Combust. Flame*, 80(2):135–149, 1990.

[31] J. H. Kent and D. Honnery. Soot and mixture fraction in turbulent diffusion flames. *Combust. Sci. Technol.*, 54:383–397, 1987.

[32] H. Koseki. Combustion properties of large liquid pool fires. *Fire Technology*, 25:241–255, 1989.

[33] E. R. Hawkes, R. Sankaran, J. C. Sutherland, and J. H. Chen. Scalar mixing in direct numerical simulations of temporally-evolving plane jet flames with detailed CO/H_2 kinetics. *Proc. Combust. Inst.*, 31:1633–1640, 2007.

[34] E. Effelsberg and N. Peters. Scalar dissipation rates in turbulent jets and jet diffusion flames. *Proc. Combust. Inst.*, 22:693–700, 1988.

[35] A. N. Karpetis and R. S. Barlow. Measurements of flame orientation and scalar dissipation in turbulent partially premixed methane flames. *Proc. Combust. Inst.*, 30:665–672, 2005.

[36] C. Pantano, S. Sarkar, and F. A. Williams. Mixing of a conservered scalar in a turbulent reacting shear layer. *J. Fluid Mech.*, 481:291–328, 2003.

[37] C. H. Gibson. Fine structure of scalar fields mixed by turbulence. I. zero-gradient points and minimal gradient surfaces. *Phys. Fluids*, 11(11):2305–2315, 1968.

[38] S. B. Pope. The evolution of surfaces in turbulence. *Int. J. Engng. Sci.*, 26(5):445–469, 1988.

[39] T. Echekki and J. H. Chen. Analysis of the contribution of curvature to premixed flame propagation. *Combust. Flame*, 118:308–311, 1999.

[40] C. H. Gibson. Turbulence in the ocean, atmosphere, galaxy, and universe. *Applied Mechanical Review*, 49:299–315, 1996.

[41] A. Y. Klimenko and R. W. Bilger. Conditional moment closure for turbulent combustion. *Prog. Energy Combust. Sci.*, 25:595–687, 1999.

[42] A. Kronenburg and R. W. Bilger. Modelling of differential diffusion effects in nonpremixed nonreacting turbulent flow. *Phys. Fluids*, 9:1435–1447, 1997.

[43] J. C. Hewson, A. J. Ricks, S. R. Tieszen, A. R. Kerstein, and R. O. Fox. Conditional moment closue with diferential diffusion for soot evolution in fire. *Center for Turbulence Reseach, Proceedings of the Summer Program*, 2006.

[44] A. Kronenburg, R. W. Bilger, and J. H. Kent. Modeling soot formation in turbulent methane-air jet diffusion flames. *Combust. Flame*, 121:24–40, 2000.

[45] A. Beltrame, P. Porshnev, W. Merchan-Merchan, A. Saveliev, A. Fridman, and L. A. Kennedy. Soot and no formation in methane-oxygen enriched diffusion flames. *Combust. Flame*, 124:295–310, 2001.

List of Figures